Supplementary Material for
Direct observation of chiral edge current at zero magnetic field in a magnetic topological insulator

Outline

S1: Method

Crystal growth

The high quality $MnBi_2Te_4$ bulk single crystals were grown by direct reaction of a 1:1 mixture of Bi_2Te_3 and MnTe in a sealed silica ampoule under a dynamic vacuum. The mixture was first heated to 973 K, then slowly cooled down to 864 K. The crystallization occurred during the prolonged annealing at this temperature.

Device fabrication

Thin $MnBi_2Te_4$ flakes were exfoliated by using the Scotch tape method onto 285 nm-thick SiO_2/Si substrates, which were pre-cleaned in air plasma for 5 minutes at 125 Pa. Before spinning-coating Polymethyl methacrylate (PMMA), the surrounding thick flakes were removed by a sharp needle. A marker array was first prepared on the substrates for precise alignment between the selected flake and the patterned electrodes. All the device fabrication processes were carried out in an argon-filled glove box with O_2 and H_2O levels below 0.1 PPM. By using electron-beam lithography, metal electrodes (Cr/Au, 5/50 nm) were deposited in a thermal evaporator connected to the glove box. When transferred between the glove box, electron beam lithography, and the cryostat, the devices were covered by a layer of PMMA to mitigate air contamination and sample degradation.

Transport measurement

Electrical transport measurements were carried out in a commercial cryostat Attodry 2100 with a base temperature of 1.7 K and a magnetic field of up to 9 T. The longitudinal and Hall voltages were detected simultaneously by using a lock-in amplifier (Stanford Research System 830). The bottom-gate voltages were applied by a Keithley 2400 multimeter.

Scanning SQUID measurement

Scanning SQUID measurements were carried out in the same cryostat as transport measurements. The nano-SQUID sensors used for this study were scanning 2-junction SQUID susceptometers with two balanced pickup loops of 2 μm diameter in a gradiometric configuration, each surrounded by a one-turn field coils of 10 μm diameter. These devices were planarized throughout, which minimized the spacing between the pickup loop-field coil pair and the sample surface. The SQUID is ~1 μm above the sample during the scan. The spatial resolution was limited by both the size of the pickup loop and the height of it from the sample.

For the scanning SQUID measurements throughout this paper, we employed two different modes to probe magnetic properties. Magnetometry (Φ) is a DC measurement of flux through the pickup loop as a function of position and shows the intrinsic magnetization of the sample. Because the pickup loop is parallel to the sample surface, it is only sensitive to the local out-of-plane magnetic field. The magnetometry was performed simultaneously with current flux imaging. The DC static flux signal was measured using a voltage meter (Zurich Instrument HF2LI), while the current flux signal generated by the AC + DC current flowing through the device was demodulated using a lock-in amplifier (Stanford Research System 830), and the frequency of the AC current bias is 155.55 Hz for the current flux images shown in the main text unless otherwise stated.

S2: Spatial resolution of sSQUID

For vortices in thick Nb films, the dispersion range of the magnetic signal produced is much smaller than the resolution of the sSQUID. This allows us to consider it as a magnetic monopole on the surface of the Nb film. The extent of dispersion of the magnetic signal from the vortex obtained by sSQUID measurements reflects the spatial resolution of the measurement system. Figure S1a shows the static magnetic flux image of an isolated vortex on a 400 nm thick Nb film. Along the linecut indicated by the grey dashed arrow shown in Figure S1a, the FWHM of the Lorentzian fit of linecut shown in Figure S1b is approximately 2.12 μm, indicating that the spatial resolution of our sSQUID is approximately 2.12 μm.

Additionally, the width of the magnetic signal of the step between a Nb film and non-magnetic substrate changing from 25% to 90% can also serve as a criterion for assessing the spatial resolution of the sSQUID. Figure S1c shows the static magnetic flux image of a 5 μm Nb chess pattern indicated by the inset of Figure S1d. Analysis of the line cut of the step signal of Nb squares in Figure S1c yields a spatial resolution of approximately 2.57 μm for our sSQUID, consistent with the resolution level determined by the isolated superconducting vortex image.

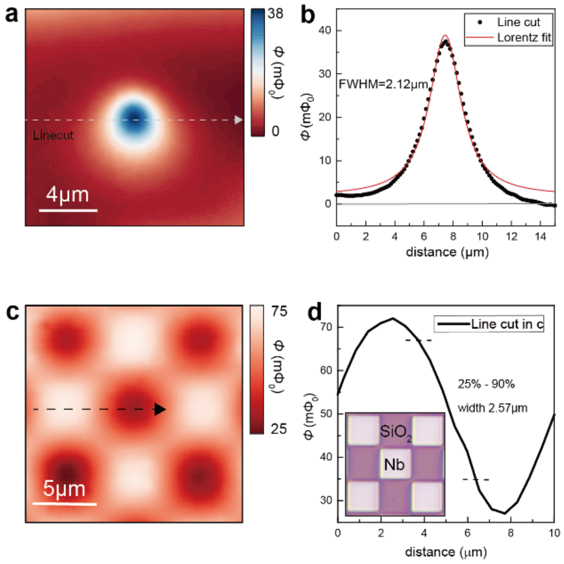

FIG. S1 Spatial resolution of sSQUID. a, Static magnetic flux image of an isolated vortex on a 400 nm thick Nb film. **b**, Line cut and Lorentzian fit along the grey dashed arrow in **a**. **c**, Static magnetic flux image of a 5 μm Nb film chess pattern. **d**, Line cut along the black dashed arrow in **c**, inset: optical image of the 5 μm Nb chess corresponding to the area in **c**.

S3: Current Inversion

In this section, we will give a description of the current inversion process [1,2] in more detail.

We treat the 7-SL MnBi2Te4 flake device as a quasi-two-dimensional thin sheet with thickness of d, and assume the current flowing through the Hall bar device is quasi-static ($\nabla \cdot \boldsymbol{J} = 0$) and confined in the thin sheet of thickness d (we assume it to be the *x-y* plane at *z* = 0). Based on the assumption, we can neglect the J_z and the *z* dependence of J_x and J_y.

In the scanning SQUID experiment, we scan the SQUID pick-up loop at a height of z ($z \gg d$) from the Hall bar device, and the pick-up loop will collect the *z* component of the magnetic flux generated by the current flowing through the Hall bar, which can be derived from the Biot-Savart law:

$$B_z(x,y,z) = \frac{\mu_0 d}{4\pi} \iint \frac{J_x(x',y')(x-x') - J_y(x',y')(y-y')}{((x-x')^2 + (y-y')^2 + z^2)^{\frac{3}{2}}} dx'dy' \tag{1.}$$

A convolution expression can be obtained by applying a two-dimensional Fourier transform to both sides of the equation:

$$b_z(k_x,k_y,z) = j_x(k_x,k_y) g_y(k_x,k_y,z) + j_y(k_x,k_y) g_x(k_x,k_y,z) \tag{2.}$$

$$g_y(k_x,k_y,z) = \mathcal{F}_{xy}\left[\frac{\mu_0 d}{4\pi} \frac{(y-y')}{[(x-x')^2 + (y-y')^2 + z^2]^{\frac{3}{2}}}\right] \tag{3.}$$

$$g_x(k_x,k_y,z) = \mathcal{F}_{xy}\left[\frac{\mu_0 d}{4\pi} \frac{-(x-x')}{[(x-x')^2 + (y-y')^2 + z^2]^{\frac{3}{2}}}\right] \tag{4.}$$

Where j_x, j_y and b_z are the two-dimensional Fourier transformations of current density J_x, J_y and magnetic field B_z. We also notice that the current density obeys the quasi-static condition ($\nabla \cdot \boldsymbol{J} = 0$), which in transform space becomes:

$$-ik_x j_x(k_x,k_y) - ik_y j_y(k_x,k_y) = 0 \tag{5.}$$

Combining equations (2) - (5), we can get the Relational expression between j_x, j_y and b_z:

$$j_x(k_x,k_y) = i\frac{\mu_0 d}{2} \frac{k_y\sqrt{k_x^2 + k_y^2}}{k_x^2 + k_x k_y} \exp\left(\sqrt{k_x^2 + k_y^2} z\right) b_z(k_x,k_y,z) \tag{6}$$

$$j_y(k_x,k_y) = i\frac{\mu_0 d}{2} \frac{k_x\sqrt{k_x^2 + k_y^2}}{k_y^2 + k_x k_y} \exp\left(\sqrt{k_x^2 + k_y^2} z\right) b_z(k_x,k_y,z) \tag{7}$$

Finally, we can get the real-space current density distribution J_x and J_y by performing an inverse Fourier transformation on j_x and j_y, and the total current density J is also obtained ($J = \sqrt{J_x^2 + J_y^2}$).

We begin with the out of plane component of the magnetic field B_z generated by the current in the above inversion procedure. But scanning SQUID actually collects the magnetic flux $\phi(x, y)$ penetrates the pick-up loop, which is given by a convolution of $B_z(x, y, z_0)$ with the point spread function (PSF), $P_{\mathrm{SQUID}}(x, y)$, of the SQUID pick-up loop.

$$\phi(x, y) = \iint B_z(x', y') P_{\mathrm{SQUID}}(x' - x, y' - y) dx'dy' \tag{8}$$

The point spread function of the SQUID pick-up loop can be obtained by the magnetic flux profile $\phi_{\mathrm{M}}(x, y)$ of an isolated vortex in a bulk superconductor. The magnetic field generated by a vortex $B_{\mathrm{S}}(x, y)$ can be approximated by the field generated by a magnetic monopole, $B_{\mathrm{S}}(x, y, z) = \frac{\Phi_0 z}{(x^2+y^2+z^2)^{3/2}}$. According to equation (8) we can derive the expression of $P_{\mathrm{SQUID}}(x, y)$:

$$P_{\mathrm{SQUID}}(x, y) = \mathcal{F}^{-1}\left(\frac{\phi_{\mathrm{M}}(k_x, k_y)}{B_{\mathrm{S}}(k_x, k_y)}\right) \tag{9}$$

Figure S2 shows the PSF image calculated from the isolated vortex image in Figure S1a.

The reconstructed current density distribution will slightly deviate from the expected current flow path; as shown in Fig. 3f and h, the current density has a non-zero value out of the Hall bar device, and a dip can be seen in the current density line cut in Fig. 3h. The origin of these errors lies in the finite size of the magnetic flux image, which means we do not get the complete magnetic flux information generated by the applied current. To reduce this boundary effect, we pad out each image to a larger size (typically double the size) and linearly extrapolate the flux signal gradually to zero.

Another error introduced by the finite size of the image comes from the quasi-static current assumption ($\nabla \cdot \boldsymbol{J} = 0$). The quasi-static assumption requires that $\oint_S \boldsymbol{J} \cdot d\boldsymbol{S} = 0$ for any contour S within the image, the current inversion process introduced before will produce a finite current density outside the Hall bar geometry boundary to fulfill this condition.

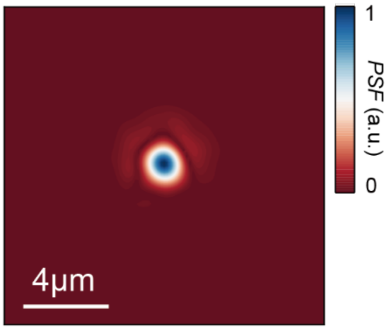

FIG. S2 Point Spread Function (PSF) image. SQUID point spread function extracted from the superconducting vortex shown in Figure S1a.

S4: Transport simulations for R_{xx} and R_{yx}

The chirality, as the remarkable character of chiral edge state surrounding a two-dimensional topological matter, is confirmed by the scanning SQUID imaging of current distribution on the device made from $MnBi_2Te_4$ flake in the manuscript. However, besides the observed chirality of edge state, such a device should in principle hold a quantized anomalous Hall effect. To explain the absence of quantization, we simulate the resistance (conductance) based on the observed chiral edge state.

Before simulation, it is necessary to mentioned the origin of Hall conductivity σ_{xy} from multiple perspectives. The quantization in Hall conductivity σ_{xy} was originally predicted without the concept of edge state by emphasizing higher Born scattering approximation under strong magnetic field [3]. After the first experimental observation [4], to interpret the quantization, a finite 2D system of annular geometry [5] without globally closed boundaries (with periodic and open boundary condition [6] in each orthogonal direction respectively) is first considered: due to the phase rigidity and the existence of mobility gap, quantization can be derived from gauge invariance [5]. The derivation for quantization in the annular geometry model [5] does not contain edge states. Supplementing this picture, edge state is explicitly solved that currents in counter directions along opposite edges contribute a net current proportional to the inner-outer Fermi level difference which is consistent with the quantization [7]. Thus, quantization and chiral edge state are related, and both of them can be attributed to the same origin. To clarify the insensitivity of quantization to boundary condition, an alternative approach is to derive the expression for σ_{xy} using linear response theory and Kubo formula [8] in an infinite periodic potential without edges [9]. Following the infinite periodic argument [9], the quantization in a finite torus [5,7] can be mapped to an adiabatic pump effect [10]. The result for σ_{xy} in infinite system [9] is an integral representing the Chern number of the U(1) bundle (vortices) defined on the magnetic Brillouin zone [11], which will turns into the winding number of edge states if the system becomes finite [12] with open boundary condition. Different from the ideal conductor for either annular geometry model [5] or infinite periodic model [9], a typical open conductor in QHE experiment is larger than the inelastic-scattering length [13], in contradiction with the phase rigidity [5,7] and its induced phase sensitive effect [14] which requires the path of carriers to enclose the Aharonov-Bohm flux [15]. To elucidate the quantization in a realistic open macroscopic sample, a confining potential gives the driving force of continuous moving edge state [13] against impurities and leads to the topologically robust quantization despite both elastic and inelastic scattering [13].

It has been visualized by magnetic imaging that in the quantum anomalous Hall regime current flows through the bulk rather than along the edge of a Hall bar device made from Cr-$(Bi, Sb)_2Te_3$ film [16]. The measured potentials at the boundaries can be well simulated by solution of Laplace's equation in which the current flows through the two-dimensional bulk with uniform conductivity tensor [17]. Both the experimental observations support the argument of bulk current flow rather than edge current applied to quantum Hall system. However, because the CES is no doubt observed by scanning SQUID method, the devices made from $MnBi_2Te_4$ flakes in this manuscript are more similar to the continuous moving edge model [13] in which the chiral edge states cannot be fully localized by weak disorder [7], and gives rise to the suppression of backscattering [13]. Therefore, our simulation is mainly based on the Landauer-Büttiker (LB) formulism for multi-terminal device [13].

Landauer-Büttiker Formulism

In transport experiment, for a given applied current, the measurement of R_{xx} and R_{yx} is equal to detecting the voltage drop between to electrodes $V_i - V_j$. The device shown in the manuscript is seen as a two-dimensional system with topologically protected chiral edge channels, on which the Landauer-Büttiker (LB) multi-terminal model is constructed [13]. for a general multi-terminal device LB equation requires

$$I_i = \frac{e^2}{h} \sum_j \left(T_{ji} V_i - T_{ij} V_j \right) = \sum_j \left(G_{ji} V_i - G_{ij} V_j \right) \tag{10}$$

where I_i is the current flowing out of the ith electrode into the sample region, V_i is the voltage on the ith electrode, and T_{ij} is the transmission probability from the jth to the ith electrode. For a chiral topological edge state, the chirality is reflected in the assigned value of T_{ij}. To be specific, the transmission probability between neighboring terminals is 1 while the others vanish. Moreover, if T_{ij} is 1, the reversed one T_{ji} is 0 due to the chirality. For a typical 6-terminal Hall bar device as shown in Figure S3, the above LB equation can be expressed as the following:

$$\begin{pmatrix} I_1 \\ I_2 \\ I_3 \\ I_4 \\ I_5 \\ I_6 \end{pmatrix} = \frac{e^2}{h} \begin{pmatrix} 1 & 0 & 0 & 0 & 0 & -1 \\ -1 & 1 & 0 & 0 & 0 & 0 \\ 0 & -1 & 1 & 0 & 0 & 0 \\ 0 & 0 & -1 & 1 & 0 & 0 \\ 0 & 0 & 0 & -1 & 1 & 0 \\ 0 & 0 & 0 & 0 & -1 & 1 \end{pmatrix} \begin{pmatrix} V_1 \\ V_2 \\ V_3 \\ V_4 \\ V_5 \\ V_6 \end{pmatrix} \tag{11}$$

If the vector of voltage drops is given, one can easily calculate the vector of current. Conversely, if one need to calculate the vector of voltages from a given current condition, one has to add an additional equation of voltages such as $V_4 = 0$ because usually the zero point of electric potential is artificially selected. However, to fit a real device the model has to be modified to meet some conditions.

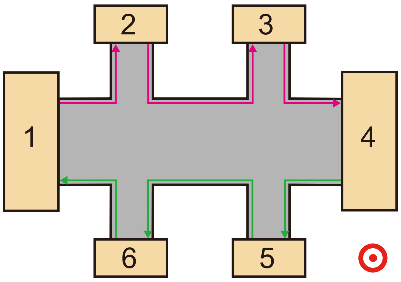

FIG. S3 Typical 6 terminal Hall bar device with chiral edge state. The magenta (green) arrows indicate the chiral current flow path of the top (bottom) edge of the Hall bar device. And the magnetization of the device is pointing out of the plane.

Modification 1: Finite edge-bulk scattering

The original multiterminal LB equation only works for ideal devices, in which the carriers moving along the edge of the device, cannot reverse direction even scattered at an impurity or by an inelastic event. Under the action of the driving force provided by the confining potential (which is positive correlated to the effective size of exchange gap), the carriers will continue to move along the edge of the device, providing current-carrying channels despite elastic and inelastic scattering. However, in this work, the exchange gap device zero field is not large enough to provide confining potential against disorder. Once the scattering at an impurity happens, the carrier has a chance to lose its velocity along the edge and enters the bulk of the device. Therefore, we must also include the edge transport dissipation due to a finite edge-bulk scattering.

Assuming the inelastic scattering happens every other distance, from the perspective of LB equation, the scattering centers play the same role as the electrodes. Since the scattering centers are evenly distributed along the device boundary and the adjacent two of scattering centers keep a certain interval, the LB equation must evolve to an advanced version with even more terminals. The number of terminals, as well as the rank of the matrix, is as much as the sum of electrodes and scattering centers.

To let the simulation program to identify the electrodes and scattering centers in optic image, we convert the optic image into a multi-dimensional array in specific format in which each electrode and each pixel along the edge are labeled by distinguishable color code, as shown in Figure S4.

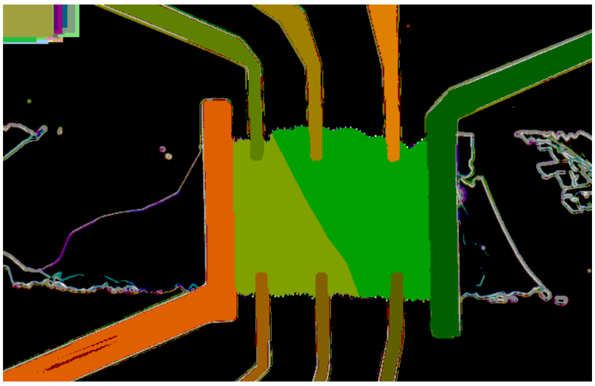

FIG. S4 Converted optic image of device#1 in 256-color mode. Within the optic image, there are different parts, including but not limited to the 7-SL area, the 10-SL area, all the electrodes, and scattering center along the boundary of the thin flake device. Each of them is identified by a specific color.

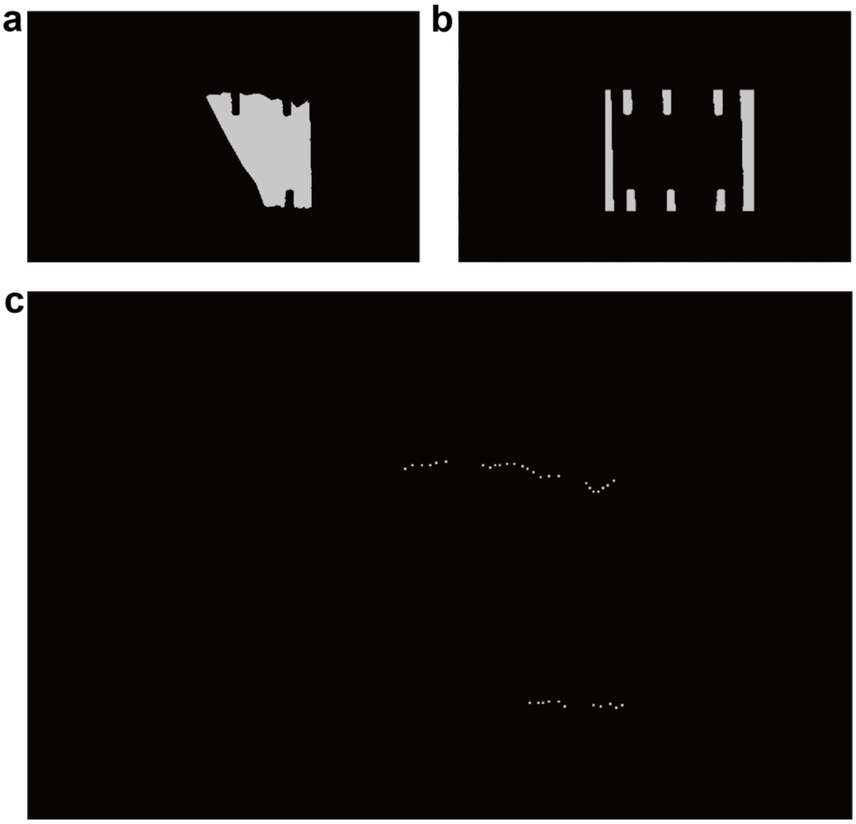

FIG. S5 Identification of converted optical image by simulation program. a, The 7-SL area of thin flake device. **b**, electrode area Au contact. **c**, the boundary of the 7-SL area of thin flake device, along which the scattering centers are distributed with certain intervals. The distance between two neighboring scattering center is just as long as the mean free path of carriers in edge channel. Since the 10-SL area is very conductive in the whole gate range, it is treated as an area in metallic phase, like electrode.

Modification 2: Bulk conduction

Second, non-zero transmission matrix elements between any two terminals must be allowed to meet the reality that electrons can hop through the bulk between each pair of electrodes. Taking these pre-conditions into consideration, one can determine the voltage on each terminal that concludes the simulation of V_{ij} for an ideal quantum Hall system with chiral edge states.

To consider the effect of finite bulk conductivity on the quantum transport, the above LB equation has to be modified. In particular, we treat the conductive bulk as parallel current flowing channels which gives rise to finite transmission probability $G_{\text{bulk}} = \left[G_{ij|\text{bulk}}\right]$. Its physical meaning is the probability that a current emitted from the jth electrode goes through the bulk of the device and enters into the ith electrode. Therefore, the total conductance matrix is:

$$G = G_{\text{edge}} + G_{\text{bulk}} = \left[G_{ij}\right] + \frac{e^2}{h}\left[T_{ij}\right] \tag{12}$$

To determine the element in the conductance matrix $[G_{ij}]$ for modified LB equation simulation, we can define the item of bulk contribution $G_{ij}|_{\mathrm{bulk}} = \sigma \int_{\Gamma_i} dr \frac{\partial U_j}{\partial \vec{n}}$ as the bulk conductance matrix where Γ_i is the interface between the device and the ith electrode, σ is the uniform bulk conductivity which can also be denoted as σ_{bulk} elsewhere and U_j is the steady-state of the electric potential $U(r)$ at the jth electrode.

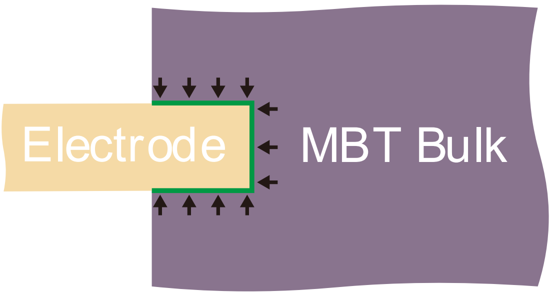

FIG. S6 Interface between bulk and electrode. The green solid line denotes the interface between the purple $MnBi_2Te_4$ bulk and the yellow electrode. Right outside the green solid line and pointing towards the electrode, the black arrows indicate the current flow direction.

To get the electric potential $U(r)$ in a 2D system made from the resistive material (uniform conductivity σ) with a static current distribution, we numerically solve the Laplace equation $\nabla^2 U = 0$ with several boundary conditions enforced. For example, the net current flowing into the Hall bar device from a voltage lead is

$$I = -\int_{\Gamma} dr \, \vec{J} \cdot \vec{n} = \sigma \int_{\Gamma} dr \frac{\partial U}{\partial \vec{n}} \tag{13}$$

The zero current condition $I = 0$ for the voltage lead is equivalent to $\int_{\Gamma} dr \frac{\partial U}{\partial \vec{n}} = 0$. Also at the voltage lead, $U|_{\Gamma} = const = U_c$. Figure S7 shows the calculated electric potential $U(r)$ corresponding to the optical image of the Hall bar device when current flows between terminal EA or AE.

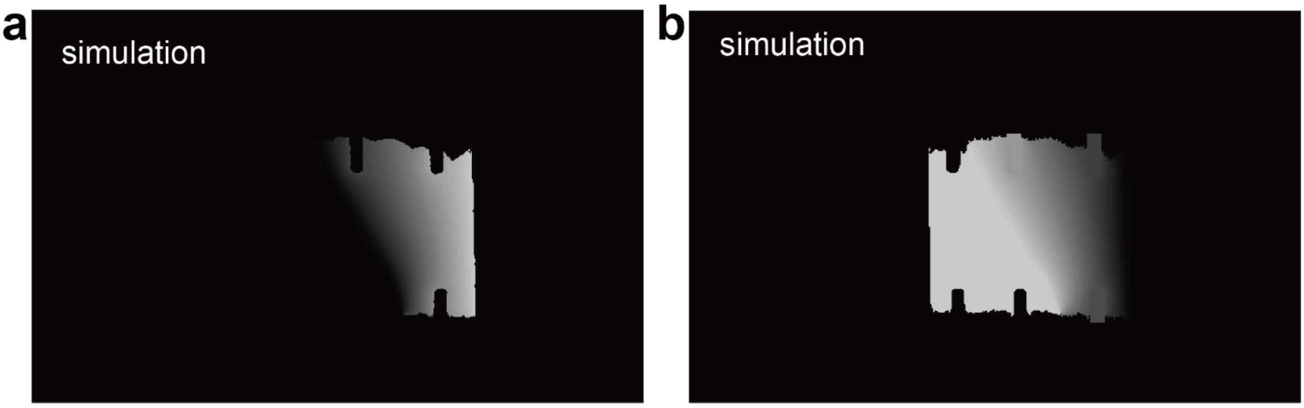

FIG. S7 The calculated electric potential $U(r)$ on the Hall bar device. **a**, high level: terminal E, ground: terminal A. **b**, high level: terminal A, ground terminal E. The calculation shown here assumes the current flowing between drain and source lead, with all the voltage leads floated, and a uniform sheet conductivity for a specific thickness. The result of the electric potential distribution is shown overlaid on an optic image of the device. The black lines indicate equipotential.

Given such $U(r)$ for all the possible pairs of generalized terminals, including electrodes A to E and scattering centers along the edge as shown in Figure S5c, we can obtain the bulk conductance matrix $\left[G_{ij|\text{bulk}}\right]$. Note that σ is unknown before simulation, however, σ can been seen as the common coefficient of all the bulk conductance $[G_{ij}]$ matrix element after merging homogeneous items, and is set as an input parameter of following simulation steps. Next, the total modified matrix $G = G_{\text{edge}} + G_{\text{bulk}} = \left[G_{ij}\right] + \frac{e^2}{h}\left[T_{ij}\right]$ can also be determined. Then by solving the LB equation, the voltage drops between any pair of terminals can be achieved.

The entire 'fitting' procedure:

Regarding the input taken from the sSQUID images, we only used the qualitative conclusion that the chiral edge state exists in the system, without employing any quantitative results from the sSQUID images. The existence of chiral edge state is contained in the LB theory in its the basic form, and then considering the introduction of some other assumptions as introduces above: bulk-edge coupling and bulk conductivity. The voltage dependence of ρ_{xx} is employed as the fitting target, while the voltage dependence of ρ_{yx} serves as means to validate the selection of N.

The fixed parameters in simulation are:

(1) LB equation itself and the edge transmissions it contains.

(2) The sample shape converted from the optical image

(3) The assumption that the bulk conductivity is uniform, allowing for the calculation of the bulk conductivity from LaPlace's equation.

The free parameters are:

(1) The number of virtual contacts (N) between actual contacts G and H, which reflects the spacing between virtual contacts. All virtual contacts are evenly distributed along the edge of the system.

(2) The bulk conductivity ($\sigma_{\text{bulk,N}}$) with respect to V_{g}. The input variable array consists of two columns.

The precise quantity being minimized in the simulation is:

the discrepancy between the simulated ρ_{xx} and the experimentally measured ρ_{xx} at each V_{g}.

The overall fitting procedure is as follows:

Once the value of N is chosen, the set of bulk conductivity ($\sigma_{\mathrm{bulk,N}}$) with respect to V_{g} will be obtained by fitting ρ_{xx} vs V_{g}. We employ the result of ($\sigma_{\mathrm{bulk,N}}$ vs V_{g}) to generate ρ_{yx} vs V_{g}. If the simulated ρ_{yx} vs V_{g} deviates from the measured R_{yx} vs V_{g} data, we opt for a larger N. Ultimately, N = 12 is concluded. For example:

(1) For the N = 2 model (N is the number of virtual electrodes added between adjacent real electrodes G and H), we fit the experimental data to obtain a set of bulk conductivity ($\sigma_{\mathrm{bulk,N=2}}$ vs V_{g}), which, as input, allows the model to output a set of $\rho_{\mathrm{xx}} - V_{\mathrm{g}}$ which is close to the experimental data. Then we input this set of bulk conductivity ($\sigma_{\mathrm{bulk,N=2}}$ vs V_{g}) to make the model output a set of $\rho_{\mathrm{yx}} - V_{\mathrm{g}}$, which we compare with the experimental data, especially the ρ_{yx} near the CNP. If the simulated ρ_{yx} is too large, it indicates that we cannot simultaneously fit $\rho_{\mathrm{xx}} - V_{\mathrm{g}}$ and $\rho_{\mathrm{yx}} - V_{\mathrm{g}}$ data in the case of N = 2.

(2) We switched to model with larger N. For the model with a larger N, we obtained a set of bulk conductivity (for example, $\sigma_{\mathrm{bulk,N=4}}$ vs V_{g}) to fit $\rho_{\mathrm{xx}} - V_{\mathrm{g}}$. However, we could not use the obtained ($\sigma_{\mathrm{bulk,N=4}}$ vs V_{g}) to simultaneously fit $\rho_{\mathrm{yx}} - V_{\mathrm{g}}$ data, indicating that the N = 4 model is also not suitable.

(3) We continued to switch to another N…

(4) Finally, we used the N = 12 model and obtained satisfactory results. Specifically, we used the set of bulk conductivity ($\sigma_{\mathrm{bulk,N=12}}$ vs V_{g}) to obtain ρ_{xx} denoted by yellow circles in Fig. 4e and ρ_{yx} denoted by black squares in Fig. 4f.

In addition to showing the fitting result of the bulk conductivity ($\sigma_{\mathrm{bulk,N=12}}$ vs V_{g}), we also generated curves for N = 2, 4, 8 with the fixed input ($\sigma_{\mathrm{bulk,N=12}}$ vs V_{g}) to show what would happen if the mean free path of the chiral edge state increases (by increasing the spacing between virtual contacts).

the results in Fig. 4 of manuscript for N = 2, 4, 8 cases were obtained by modified LB models with different N (the number of virtual electrodes added between adjacent real electrodes G and H), with the same input variables, the bulk conductivity ($\sigma_{\mathrm{bulk,N=12}}$) with respect to Vg. In other words, the bulk conductivity ($\sigma_{\mathrm{bulk,N=12}}$) that gives the N = 12 curve was reused without re-fitting.

The results in Fig. 4e obtained from the models with N = 2, 4, 8 further visually show the different $\rho_{\mathrm{xx}} - V_{\mathrm{g}}$ curves with a fixed input ($\sigma_{\mathrm{bulk,N=12}}$). The comparison with fixed bulk conductivity indicates that $\rho_{\mathrm{xx}} - V_{\mathrm{g}}$ curves will be consistent with the experimental results, only if the spacing of the virtual contacts is appropriate. This actually gives the range of the effective mean free path of the edge state, that is $l_{\mathrm{f}} = L_{\mathrm{GH}}/(\mathrm{N}+1)$ (~ 800 nm for $l_{\mathrm{f,N=12}}$) where L_{GH}[Y1] is the distance between actual contacts G and H.

Discussion of bulk σ: simulation and measurement

In the LB approach, we manually add *N* virtual floating probes between the neighboring real ones, and set σ as an input parameter, and the simulated longitudinal resistance (Fig. 4e, orange circles) matches the experimental data exactly. However, the best fitting σ value is not equal to the ratio of V_{BH}/I_{BH} in the bulk resistance measurement by shunting all the edge current to the ground (Fig. 4a). This is because current flows into terminal H contains both bulk current I_1 and the leak current I_2 from terminal A as shown in Figure S8a. The gate dependence of the ratio between bulk current I_1 and the leak current I_2 from terminal A manifest that around CNP, bulk current has a minimum consistent with the max bulk resistance in the gap.

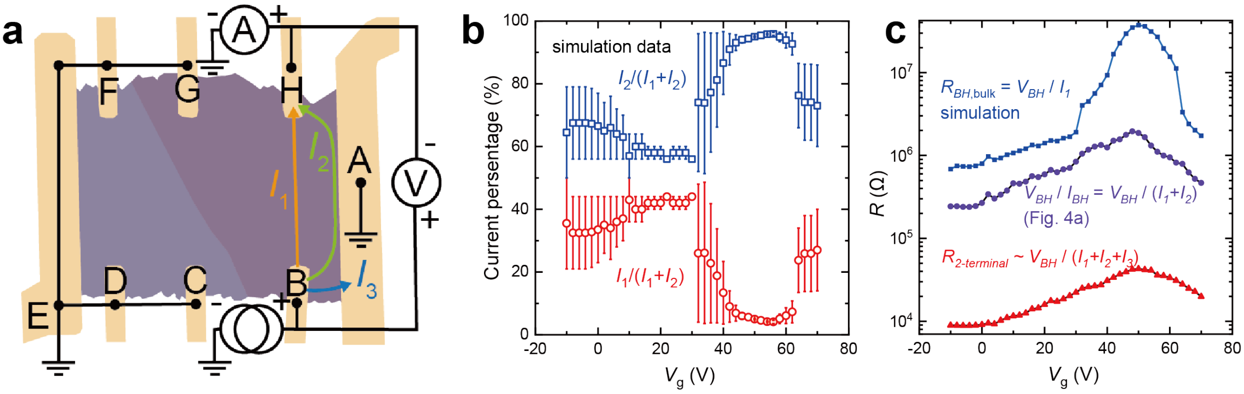

FIG. S8 The current distribution in the bulk resistance measurement. **a**, diagram of measurement setup: I_1 is the current flows into H, I_2 is the current leak from terminal A, I_3 is the current flows into terminal A. $I_1 + I_2 + I_3$ is the total current. **b**, ratio between I_1 and I_2 obtained from simulation. **c**, gate dependence of simulated bulk resistance V_{BH}/I_1, measured bulk resistance $V_{BH}/I_{BH} = V_{BH}/(I_1 + I_2)$, and two-terminal resistance between BH $R_{2-t} = V_{BH}/(I_1 + I_2 + I_3)$.

The gate dependence of simulated bulk resistance V_{BH}/I_1, measured bulk resistance $V_{BH}/I_{BH} = V_{BH}/(I_1 + I_2)$, and two-terminal resistance between BH $R_{2-t} = V_{BH}/(I_1 + I_2 + I_3)$ are summarized in Figure S6c. Although V_{BH}/I_1 is nothing but σ which is estimated from the best fitting value in resistance simulation, while the other two is measured experimentally, the result is reasonable because V_{BH}/I_1 is larger than the other two. Another important feature is the estimation of carrier density shown in Figure S9. It is based on assumption of semiconductor:

$$\sigma = e \cdot (n_e \cdot \mu_e + n_h \cdot \mu_h) \tag{14}$$

Rather than the relatively large value (red scatter) calculated from measured bulk resistance $V_{BH}/I_{BH} = V_{BH}/(I_1 + I_2)$, the estimation of carrier density based on simulated bulk resistance V_{BH}/I_1 is less than 10^{12} cm^{-2} around CNP, consistent with previous reported value [18], which also manifests the fit plausibility of simulation.

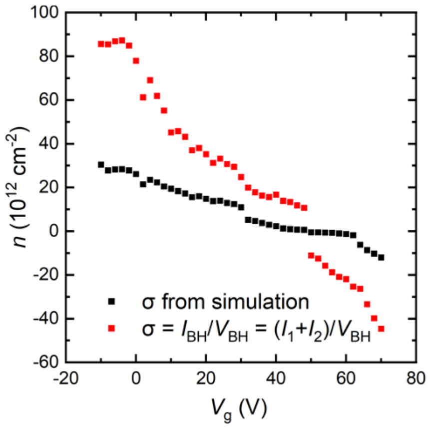

FIG. S9 The gate dependence of estimated carrier density. Black, estimated from simulated bulk resistance V_{BH}/I_1. Red, estimated from measured bulk resistance $V_{BH}/I_{BH} = V_{BH}/(I_1 + I_2)$.

S5: Transport characterization of device #1

Here we show detailed transport characterization of the device #1, on which the sSQUID results are shown in the main text. The $MnBi_2Te_4$ crystal consists of stacked Te-Bi-Te-Mn-Te-Bi-Te septuple layer (SL) and displays an A-type antiferromagnetic (AFM) order in which the magnetic moment of Mn orders ferromagnetic (FM) within each SL and AFM between neighboring SL as shown in Extended Data Fig. 1a. The optical image of the device #1 is shown in Extended Data Fig. 1b displaying two areas of different thicknesses, 7-SL and 10-SL, as labeled. Here we mainly focus on the 7-SL area. Extended Data Fig. 1c shows the gate voltage dependent longitudinal resistivity ρ_{xx} and Hall resistivity ρ_{yx} at zero magnetic field. ρ_{xx} reaches a maximum at V_g~50 V indicating the charge neutral point (CNP). On the other hand, ρ_{yx} acquires a small value in the CNP regime and becomes zero outside of it. This gating behavior of ρ_{yx} and ρ_{xx} is in substantial contrast to that of high fields ($\mu_0 H = 9$ T) as shown in Extended Data Fig. 1d. At $\mu_0 H = 9$ T, ρ_{yx} reaches a quantized Hall plateau in the CNP regime centered at V_g ~ 50 V, whereas ρ_{xx} approaches zero, indicating the Chern insulator state at high fields. Extended Data Fig. 1e shows the field dependent measurement taken at the CNP. ρ_{yx} approaches a plateau (~ 0.91 h/e^2) when the magnetic field is larger than 6 T, accompanied by a vanishing ρ_{xx} (~ 57 Ω) corresponding to a Chern insulator state at high fields. At low fields when $|\mu_0 H| < 4$ T, ρ_{yx} quickly reduces to a small value (~ 820 Ω) and displays a magnetic hysteresis with a coercive field $\mu_0 H_c = \pm$ 280 mT. The same hysteresis can be seen in ρ_{xx} as well. Such anomalous Hall effect is consistent with a non-zero net magnetization in 7-SL $MnBi_2Te_4$ at zero field. Notably, researchers observed an external gate voltage induced sign reversal of the anomalous Hall signal ρ_{yx} in 5-SL $MnBi_2Te_4$ at zero field [19], our gate voltage measurements also find this sign reversal ρ_{yx} shown in Extended Data Fig. 1c. Near the zero field, a small hysteresis is observed at about $|\mu_0 H|$ = 0.5 T due to the uncompensated ferromagnetism in odd layer $MnBi_2Te_4$ presents a ferromagnetic spin-flop process corresponding to a reversal of spins in all layers [20,21]. At the moderate field, a sharp increase (decrease) of the ρ_{yx} (ρ_{xx}) is observed began at $|\mu_0 H|$ = 4 T, where the magnetization of 7-SL $MnBi_2Te_4$ undergoes a spin-flop transition from the AFM ground state to a canting AFM (cAFM) state. With a further increase of the magnetic field, the noncollinear magnetizations in each SL eventually reach a fully aligned FM state along the external magnetic field at about $|\mu_0 H|$ = 6 T. The transport behavior of the device #1 is similar to most of the previous transport studies of $MnBi_2Te_4$ in the sense that a well-defined Chern insulator state only develops at high fields and a quantized anomalous Hall effect (QAH) is not observed at zero field.

Figures S10a and b further shows the gate voltage dependence of the longitudinal and transverse resistivity of the 7-SL area in device #1 at selected magnetic fields. Figures S10c and d show the false color plot of R_{xx} and R_{yx} as a function of the magnetic field and the gate voltage. The Chern insulator phase only appears at high fields, whereas the 7-SL area at zero field behaves as a failed QAH.

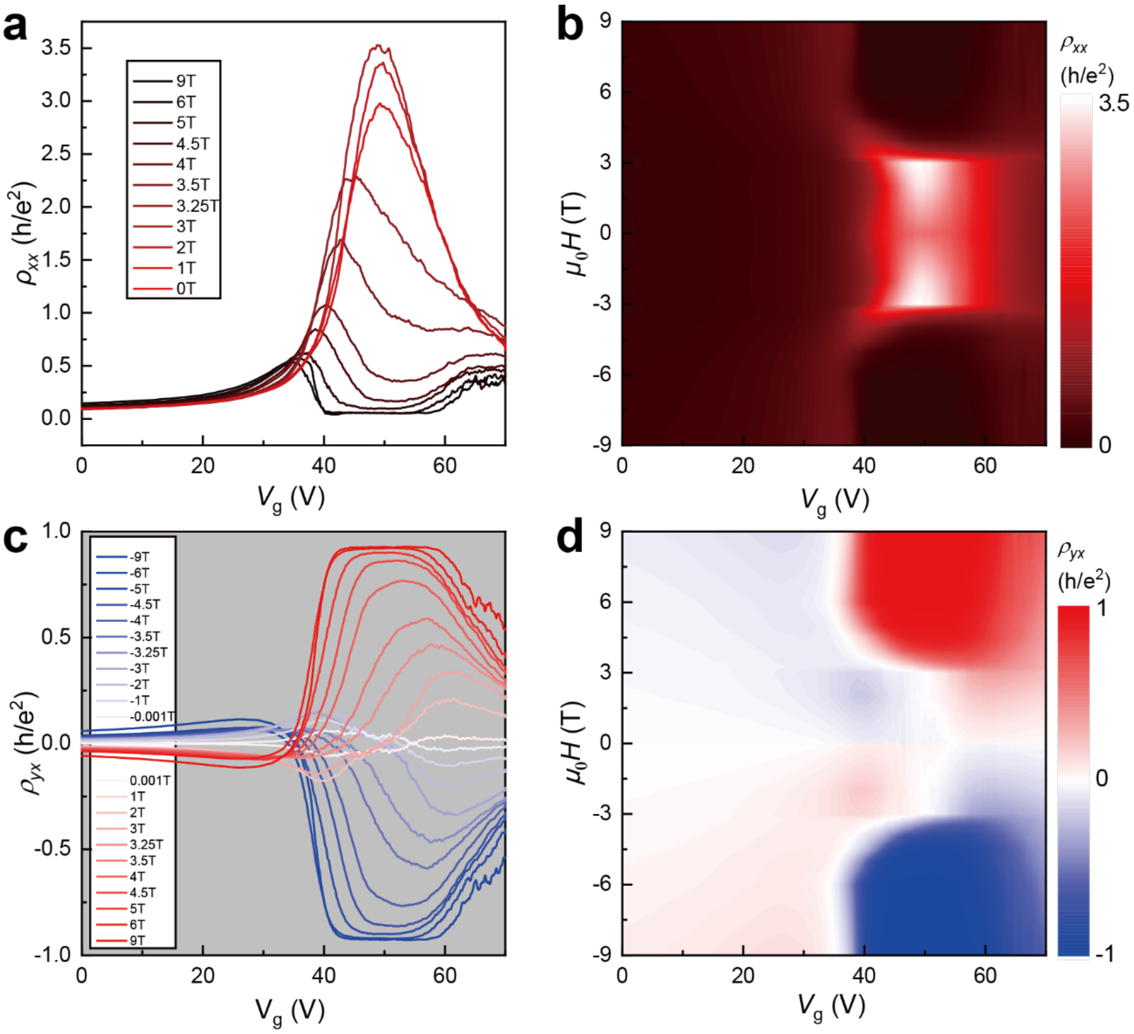

FIG. S10 Gate dependent longitudinal and transverse resistivity of device #1. a and **c**, Gate voltage dependence of ρ_{xx} and ρ_{yx} at selected magnetic fields at T = 1.7 K, respectively. **b** and **d**, Experimental phase diagram obtained by a colored contour plot of the ρ_{xx} and ρ_{yx} value at different gate voltage V_g and magnetic field $\mu_0 H$ adapted from the data in **a** and **c**, respectively.

S6: Chiral edge current detected in a different current biasing configuration in device #1

We have tried a different current biasing configuration in the scanning SQUID measurement from the one used in the main text. As shown in Figure S11, the current only flows through the 7-SL area without the influence of the 10-SL area. Figures S11a and b show the current flux image measured at $V_g = 0\ \mathrm{V}$ with an opposite current flow direction. They show a homogeneous current flow through the central bulk of the 7-SL area after one reverses the current flow direction, indicating a bulk-dominated current transport. When the Fermi level is tuned to CNP ($V_g = 50\ \mathrm{V}$) in Figures S11c and d, the current flow path moves towards the boundary of the 7-SL area. Moreover, it shows an obvious chirality. The current flows along the bottom edge and the step edge between the 7-SL and 10-SL areas in Figure S11c and changes to the top edge in Figure S10d when the source and drain electrodes are exchanged (denoted by arrows in Figs. S11c and d). In other words, the chiral edge current follows a clockwise chirality when the magnetization points out of the plane, as shown in Figures S11c and d. If one reverses the magnetization by magnetizing the device at an opposite magnetic field, such as $\mu_0 H = -9\ \mathrm{T}$ in Figures S11e and f, the chirality of the edge state is reversed to an anti-clockwise pattern. In summary, one confirms the existence of a chiral edge current in the 7-SL area whose chirality can be controlled by the magnetization direction.

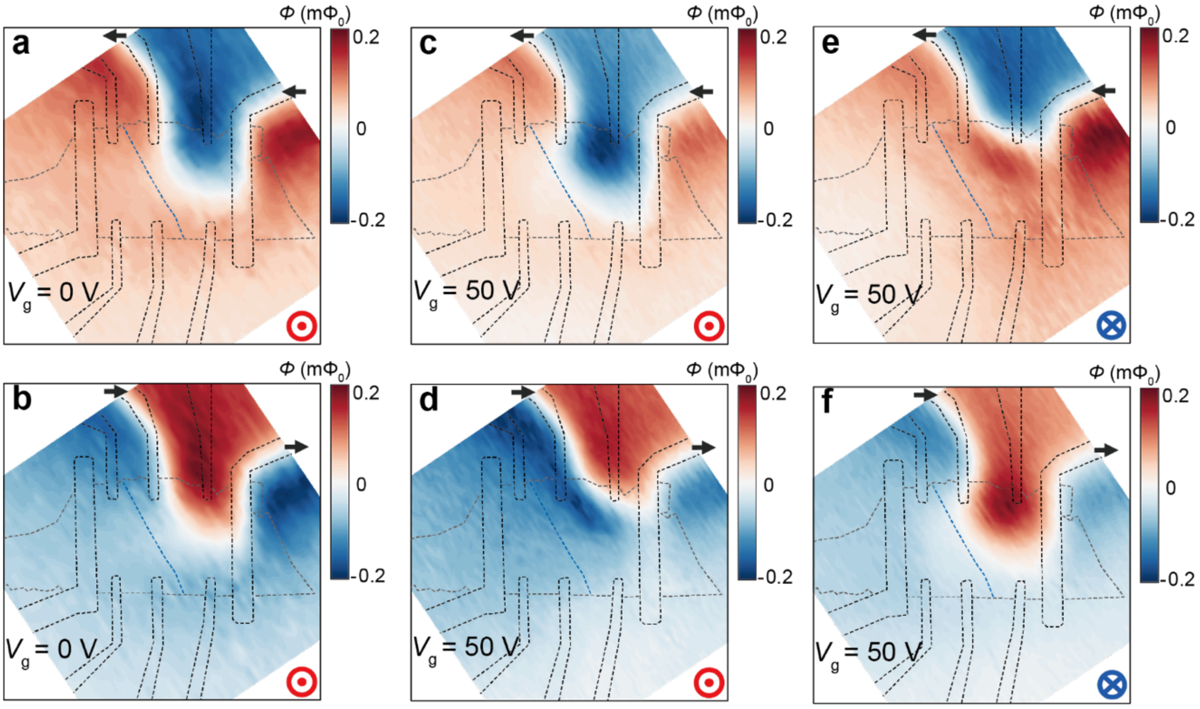

FIG. S11 Chiral edge current flowing through pure 7-SL area. **a** and **b**, Current flux images of 7-SL area at $V_g = 0\ \mathrm{V}$ with opposite bias direction. **c** and **d**, Current flux images at $V_g = 50\ \mathrm{V}$ (CNP) corresponding to the bias direction in **a** and **b**, respectively. **e** and **f**, Current flux images with the same bias direction but opposite magnetization direction in **c** and **d**, respectively.

S7: Transport characterization of device #2

We perform the transport and scanning SQUID measurements on a different $MnBi_2Te_4$ device (device #2) which consists of a 7-SL and 8-SL area as shown in Figure S12a. Figure S12 shows the transport results. Figure S12b is the field dependent ρ_{xx} and ρ_{yx} at CNP. Similar to device #1, the quantized ρ_{yx} and the vanished ρ_{xx} at high magnetic fields in the 7-SL area demonstrate a Chern insulator state in device #2. However, ρ_{yx} quickly decreases below 4 T and shows a tiny hysteresis loop around the zero field indicating a non-zero net magnetization of the 7-SL area. The same hysteresis can be resolved in ρ_{xx} as well. Figure S12c shows the gate voltage dependent ρ_{xx} and ρ_{yx} at zero field. ρ_{xx} reaches a peak at $V_g = 30$ V, and ρ_{yx} displays a non-zero small value in the gate voltage range from 20 V to 30 V. The same gate voltage dependent measurement at the high field ($\mu_0 H$ = 9 T) is shown in Figure S12d. ρ_{yx} reaches a quantized Hall plateau in the CNP regime centered at V_g ~28V where ρ_{xx} approaches zero, consistent with the high field Chern insulator behavior in Figure S12b.

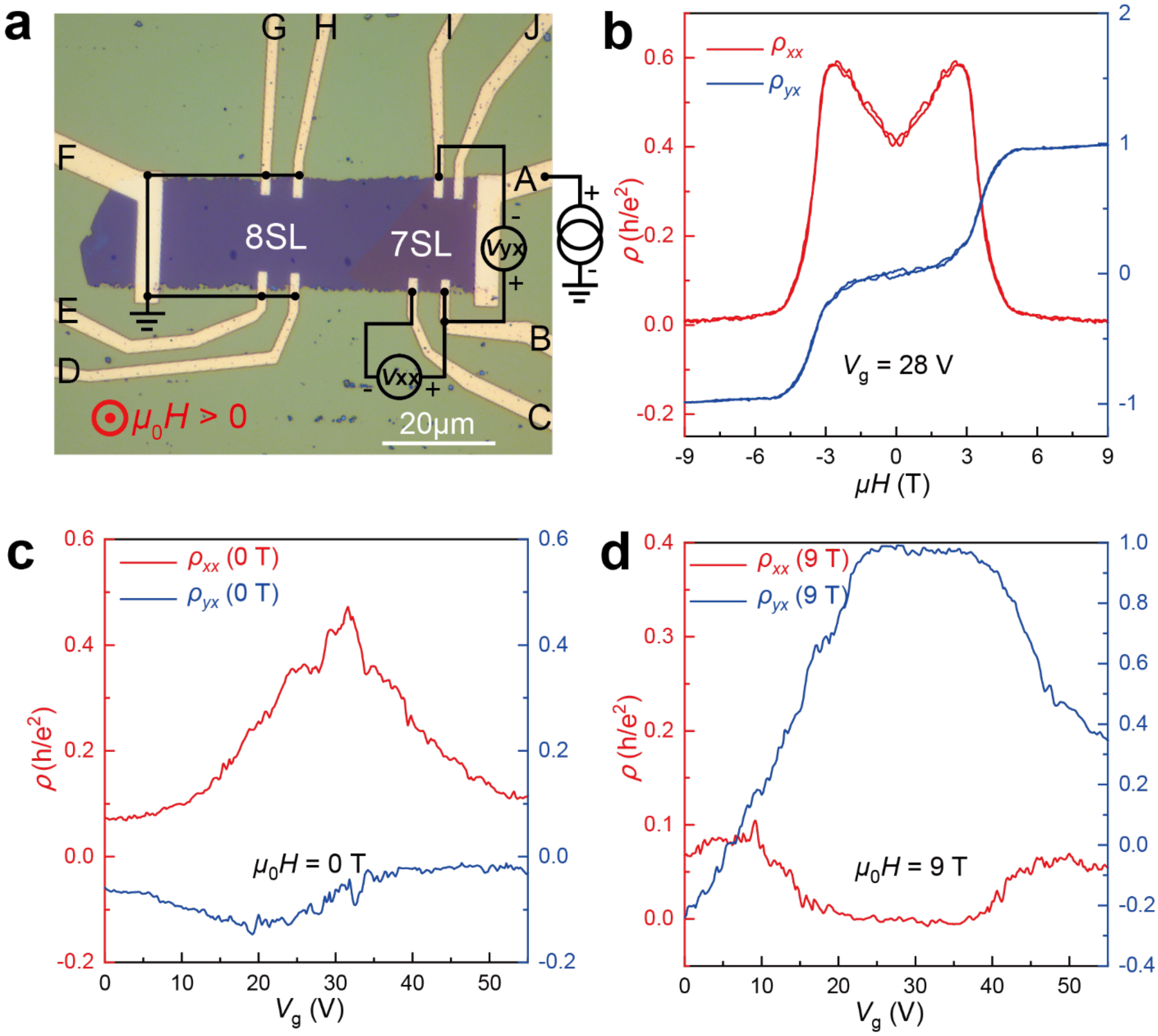

FIG. S12 Transport calibration of the 7-SL flake in device #2. **a**, Optical image of device #2 with thickness labeled by white letters. The black letters label the electrodes. **b**, magnetic field dependence of ρ_{xx} and ρ_{yx} of the 7-SL MBT flake of device #2 at $V_\mathrm{g} = 28\,\mathrm{V}$ (CNP). **c** and **d**, Gate dependent ρ_{xx} and ρ_{yx} at zero magnetic field and $\mu_0 H = 9$ T, respectively.

S8: Chiral edge current in device #2

While the transport measurement of device #2 also suggests a failed QAH state at zero field in the 7-SL $MnBi_2Te_4$, the scanning SQUID measurement indicates a chiral edge current. Figures S13a and b display the static magnetic flux maps of device #2 after an opposite initial magnetization process. While the 8-SL area shows a negligible flux signal consistent with its even-layer thickness, the 7-SL area shows an opposite flux signal, indicating a reversed magnetization direction. Figures S13c and e are the current flux images taken at CNP corresponding to the magnetization direction of Figure S13a. One reverses the biasing current direction between Figures S13c and e. The current flows along the boundary of the 7-SL area and follows a clockwise chirality. It unambiguously shows the existence of a chiral edge current in the 7-SL area. Figures S13d and f are the same measurements as Figures S13c and e, but with an opposite magnetization corresponding to the case in Figure S13b. Similar to device #1, a reversed magnetization changes the chirality of the edge current from clockwise to anti-clockwise in the 7-SL area of device #2.

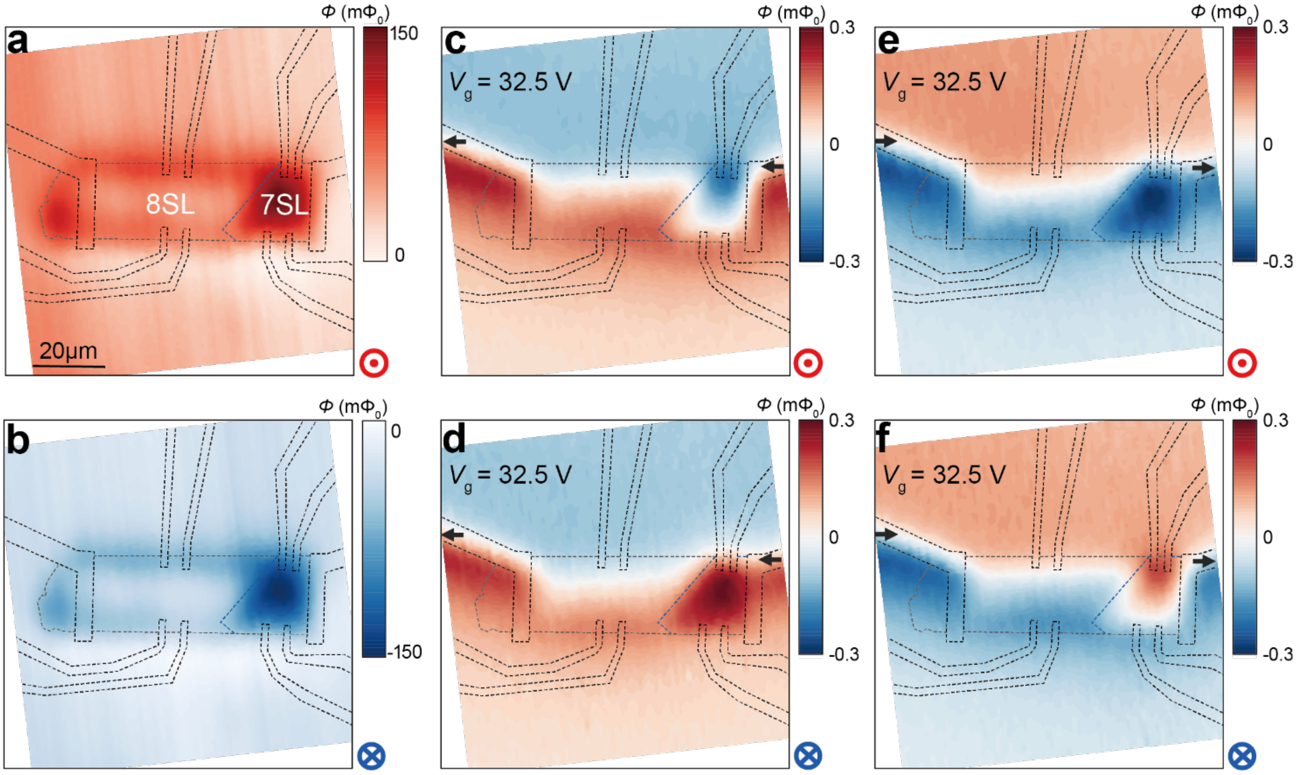

FIG. S13 Chiral edge current under opposite magnetization in device #2. a and **b**, Static magnetic flux images with the device magnetized at 9 T in **a** and -9 T in **b**. **c** and **d**, Current flux images with a 500 nA AC current plus 1 μA DC offset applied to the top electrode, corresponding to the magnetization in **a** and **b**, respectively. **e** and **f**, Current flux images with the same current bias as in **c** and **d** but applied to bottom electrode.

S9: Negative DC offset

In order to detect a chiral edge current signal, one adopts an AC+DC offset scheme as described in the main text. In particular, one applies a positive DC offset larger than the AC amplitude. However, if a negative DC offset is applied, one still gets the chiral edge current signal, but its chirality is opposite to the real one. Extended Data Fig. 2 compares two cases in device #2. The device was initially magnetized under -9 T, so the residual magnetization of the 7-SL area points into the plane as denoted in Extended Data Fig. 2a. In this case, the edge current should follow an anti-clockwise chirality, as demonstrated in Extended Data Fig. 2b with a positive DC offset. When a negative DC offset is applied (Extended Data Fig. 2c), the current flux signal demodulated by the lock-in amplifier indicates an edge current with a clockwise chirality in the 7-SL area.

S10: Pure AC current bias

To successfully detect the chiral edge current signal, a DC offset is necessary. Here we show that the chiral edge current signal is totally missed if one only applies a pure AC current bias. Extended Data Fig. 3a and b are the current flux images of device #1 demodulated by a lock-in amplifier in a pure AC current bias scheme. They manifest that the current flows through both edges along the same direction (Fig. 1g). Therefore, one has a null flux signal in the center of the 7-SL area. The chiral edge current signal is missed.

S11: Transport calibration of device#3

We perform the transport and sSQUID measurement on a pure 7-SL $MnBi_2Te_4$ device (device#3). Figure S14a shows the optical image of device#3, which has a uniform thickness between electrode A and D. The quantized ρ_{yx} and the vanished ρ_{xx} at high magnetic fields of the 7-SL flake (Figure S14b) indicate a Chern insulator state in device #3. When the magnetic field is below 4 T, ρ_{yx} decreases rapidly, showing a small hysteresis loop at zero field, indicating non-zero magnetization of the 7-SL $MnBi_2Te_4$. A similar hysteresis loop is also discernible in ρ_{xx}. Figure S14c shows the gate voltage dependence of ρ_{yx} and ρ_{xx} at the magnetic field $\mu_0 H = 9\,\mathrm{T}$. Between the gate voltage range of 0 V to 5 V, ρ_{yx} reaches the quantized resistance value, while ρ_{xx} drops to zero, indicating good sample quality in device#3.

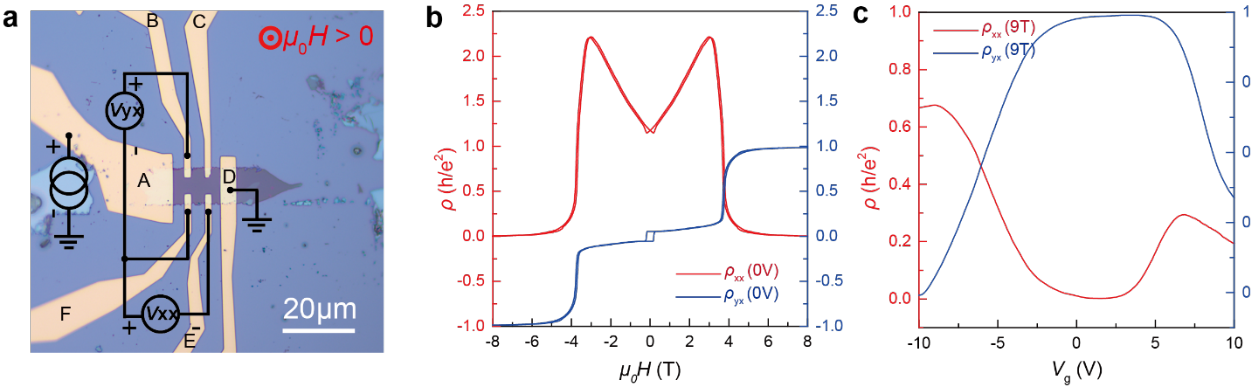

FIG. S14 Transport calibration of the pure 7-SL $MnBi_2Te_4$ device#3. **a**, Optical image of device#3. The black letters label the electrodes. **b**, Magnetic field dependence of ρ_{xx} and ρ_{yx} at $V_{\mathrm{g}} = 0\,\mathrm{V}$. **c**, Gate voltage dependence of ρ_{xx} and ρ_{yx} at $\mu_0 H = +9\,\mathrm{T}$.

S12: Chiral edge current before magnetization

The odd-layered atomic thin $MnBi_2Te_4$ flake exhibits ferromagnetic order below its Curie temperature, which breaks time-reversal symmetry (TRS) and opens a magnetic exchange gap that is crucial for the presence of the chiral edge state. However, when the odd-layered $MnBi_2Te_4$ device is cooled down under zero magnetic field, the ferromagnetic order it forms may be spatially non-uniform (which may lead to spatial variation of the magnetic exchange gap or the formation of magnetic domains), or the magnetic spins may not be fully aligned (which may lead to a not fully opened magnetic exchange gap). These conditions can weaken or even obscure the observed chiral edge current (CEC). Recent work reports only a very low magnetic field (~3 mT) applied in field cooling for odd layer $MnBi_2Te_4$ can generate a single domain [22]. Applying an external magnetic field to magnetize the sample can reduce the spatial non-uniformity of its ferromagnetism, thereby facilitating the emergence of CEC.

To verify the presence of CEC in odd layered $MnBi_2Te_4$ thin flake, we perform sSQUID measurements on device#3 before magnetization. Figure S15a shows the static flux image of the device#3 before magnetization, revealing that the magnetization intensity in the region between electrodes A and D is consistent with the magnetization intensity after being magnetized at -9 T (Figure S15c). Notably, the device#3 in Figure S15a exhibits single-domain magnetization without forming magnetic domains due to the remnant magnetic field in our system. In Figure S15b, the sample magnetized at +9 T shows magnetization intensity equal in magnitude but opposite in direction to that in Figure S15c.

The current flux images in Figures S15d and g demonstrate that device#3 maintains a chiral edge current (CEC) even before magnetization, with its chirality matching that of the device magnetized at -9 T (Figures S15f and i) and opposite to that of the device magnetized by +9 T (Figures S15e and h). Figure S15j presents the sum current flux image of Figures S15d and g. By canceling out the current flux signals from the electrode regions, we can clearly observe the net chiral current flux contributed by the CEC around the sample area. The signal strength and spatial distribution in Figure S15j align with those in the sum current flux image (Figure S15l) of Figures S15f and i, with the device magnetized at -9 T. Conversely, Figure S15k, showing the sum current flux image of Figures S15e and h, exhibits an opposite chirality due to the device being magnetized at +9 T.

From above images, it can be seen that for $MnBi_2Te_4$, before magnetization, due to the relatively low spatial non-uniformity of its spontaneously formed ferromagnetic order, we can still observe the chiral edge current (CEC).

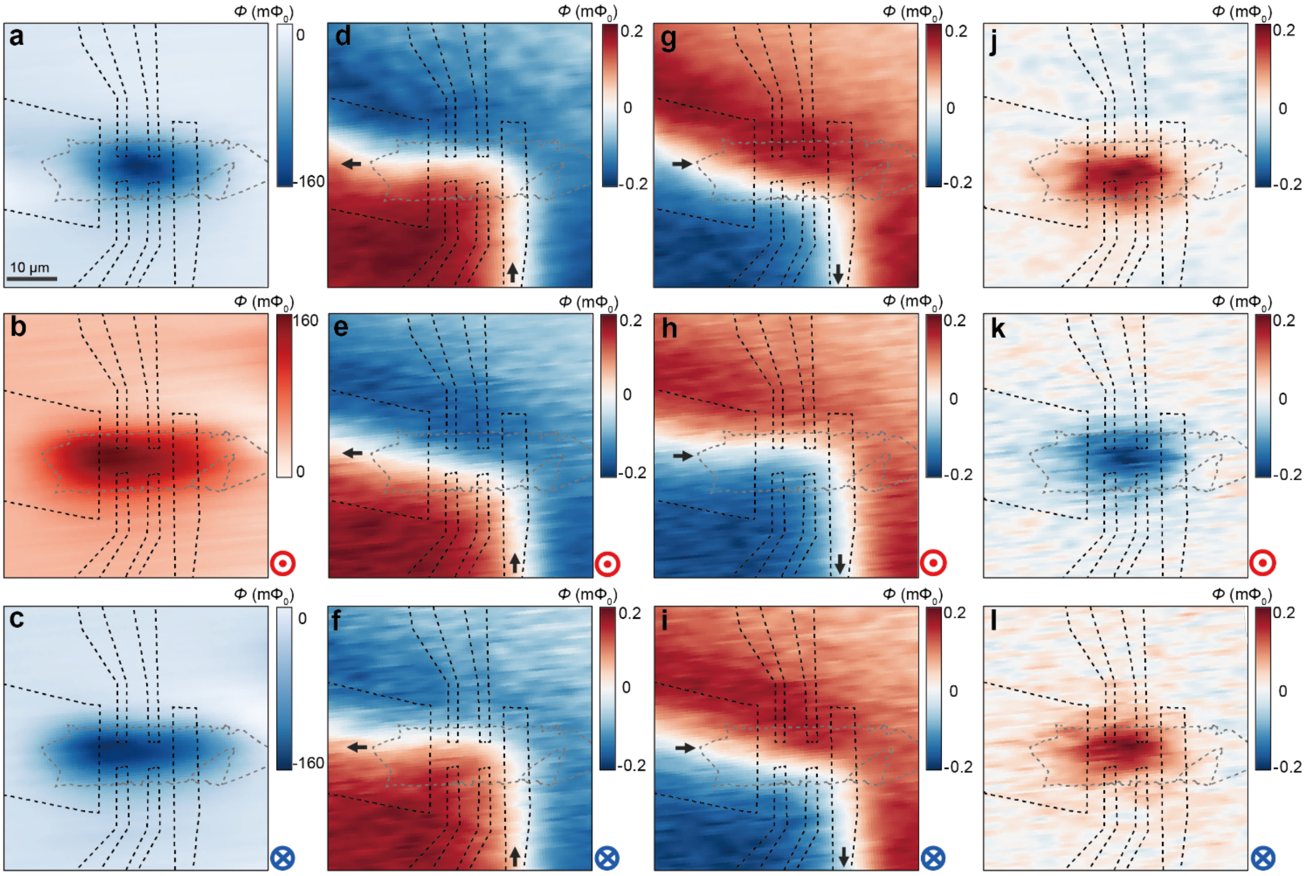

FIG. S15 Chiral edge current under zero field cooling. a, Magnetometry image of device#3 after zero field cooling, **b** and **c,** magnetometry images after applying +9 T field and -9 T, respectively. **d** to **f**, Current flux images with an AC 500 nA + DC 1 μA current bias applied to electrode D corresponding to the magnetization in **a** to **c**, respectively. **g** to **i**, current flux images with an AC 500 nA + DC 1 μA current bias applied to electrode A corresponding to the magnetization in **a** to **c**, respectively. **j** to **l**, Sum current flux images of (**d** + **g**) in **j**, (**e** + **h**) in **k** and (**f** + **i**) in **l**, respectively. All the images are taken at $V_g = 5$ V.

S13: Second harmonic magnetic flux response to the applied current

The heating effect of current flowing through the sample might affect the magnetization of $MnBi_2Te_4$ flake. By examining the second harmonic current flux images, we can reflect the influence of current-induced heating on the magnetization of $MnBi_2Te_4$. We apply an AC + DC current to device#3, and simultaneously record magnetic response at the first harmonic (current flux images shown in Figure S15) and the second harmonic (current flux images shown in Extended Data Fig. 4).

Extended Data Figs. 4c and d show the second harmonic current flux images when an AC 500 nA + DC 1 μA current (frequency 155.55 Hz) is applied to electrode D, corresponding to the magnetization of the device#3 in Extended Data Figs. 4a and b, respectively. We observe no features at the second harmonic current flux images, but noise. When we apply the AC 500 nA + DC 1 μA current to electrode A, the second harmonic magnetic response images (Extended Data Figs. 4e and f) also show only noise. This indicates that within the magnetic noise level of our sSQUID, the heating effect of the applied current do not significantly impact the magnetization of $MnBi_2Te_4$.

S14: Bias current dependence of the chiral edge current

In the main manuscript, we applied an AC 500 nA + DC 1 μA current bias to the sample to achieve a better Signal-to-Noise Ratio (SNR) of the current flux images, which may be relatively high compared to the AC 100 nA current bias used in transport measurements. To investigate the effect of different current bias amplitudes on the chiral edge current signal, we applied varying current biases to device#3 and collected the corresponding current flux images (Figure S16). It can be observed that when the current bias is AC 750 nA + DC 1.5 μA (Figures S16a and g), the chiral edge current features are consistent with those observed with an AC 500 nA + DC 1 μA current bias in Figures S16b and h. As the current bias gradually decreases from AC 750 nA + DC 1.5 μA to AC 50 nA + DC 100 nA (Figures S16a to f and Figures S16g to l), the amplitude of the current flux signal decreases progressively, and the performance of the signal-to-noise ratio deteriorates. However, the current still flows along the edges of device#3. Even when the current bias reduces to AC 50 nA + DC 100 nA (Figures S16f and l), we can still discern the features of the chiral edge current. Figures S16m and n shows the normalized current flux signal for different current biases along the line-cut indicated by the magenta / cyan arrow in Figures S16a and g, respectively. Figure S16o shows the normalized sum current flux signal of Figures S16m and n. It can be observed that all traces of different current biases collapse onto a single curve, indicating that the magnetic flux generated by the applied current is linear up to a relatively high current bias of AC 750 nA + DC 1.5 μA.

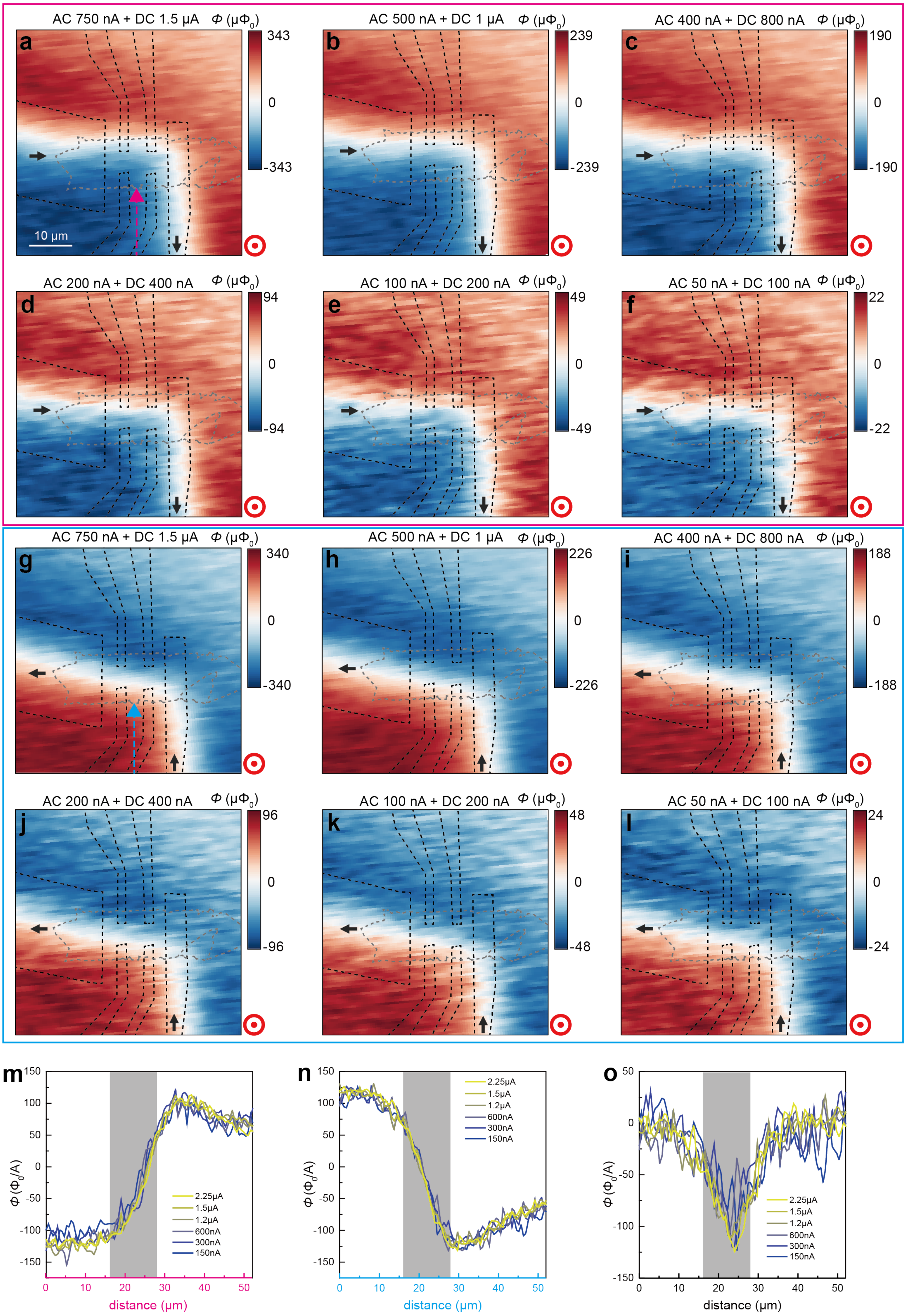
a
AC 750 nA + DC 1.5 μA
Φ (μΦ_0)
343
0
-343
10 μm
b
AC 500 nA + DC 1 μA
Φ (μΦ_0)
239
0
-239
c
AC 400 nA + DC 800 nA
Φ (μΦ_0)
190
0
-190
d
AC 200 nA + DC 400 nA
Φ (μΦ_0)
94
0
-94
e
AC 100 nA + DC 200 nA
Φ (μΦ_0)
49
0
-49
f
AC 50 nA + DC 100 nA
Φ (μΦ_0)
22
0
-22
g
AC 750 nA + DC 1.5 μA
Φ (μΦ_0)
340
0
-340
h
AC 500 nA + DC 1 μA
Φ (μΦ_0)
226
0
-226
i
AC 400 nA + DC 800 nA
Φ (μΦ_0)
188
0
-188
j
AC 200 nA + DC 400 nA
Φ (μΦ_0)
96
0
-96
k
AC 100 nA + DC 200 nA
Φ (μΦ_0)
48
0
-48
l
AC 50 nA + DC 100 nA
Φ (μΦ_0)
24
0
-24
m
150
100
50
0
-50
-100
-150
Φ (Φ_0/A)
2.25μA
1.5μA
1.2μA
600nA
300nA
150nA
0
10
20
30
40
50
distance (μm)
n
150
100
50
0
-50
-100
-150
Φ (Φ_0/A)
2.25μA
1.5μA
1.2μA
600nA
300nA
150nA
0
10
20
30
40
50
distance (μm)
o
50
0
-50
-100
-150
Φ (Φ_0/A)
2.25μA
1.5μA
1.2μA
600nA
300nA
150nA
0
10
20
30
40
50
distance (μm)

FIG. S16 Current dependence of the chiral edge current in device#3. a to **f**, Current flux images with the current bias being AC 750 nA + DC 1.5 μA down to AC 50 nA + DC 100 nA. The current bias is applied to electrode A and electrode D grounded. **g** to **l**, Current flux images with the current bias being AC 750 nA + DC 1.5 μA down to AC 50 nA + DC 100 nA. The current bias is applied to electrode D and electrode A grounded. **m** and **n**, The normalized current flux line-cuts along the magenta dashed arrow in **a** and cyan dashed arrow in **g**, respectively. **o**, The sum current flux line-cuts of **m** and **n**.

S15: Gate voltage evolution of the magnetization of device#1

The magnetization of odd-layered $MnBi_2Te_4$ is crucial for the presence of CEC. To observe the CEC, we apply a back gate voltage to tune the Fermi level of the sample, along with an AC + DC current bias. Therefore, it is essential to ensure that the applied back gate voltage and current bias do not significantly affect the magnetization of the sample.

Figure S17a shows the evolution of the static flux line-cut of the 7-SL area in device#1 with back gate voltage ranging from 0 V to 70 V, recorded simultaneously with Figure 3c. According to Figure 3c, the spatial distribution of the current in the 7-SL area of device#1 transitions from bulk dominant (Vg < 40 V) to edge dominant (40 V < Vg < 60 V) and back to bulk dominant (Vg > 60 V). However, in Figure S17a, we can see that the static flux signal of the sample remains almost unchanged across the entire range of back gate voltages. Additionally, Figure S17b shows the evolution of the static flux with back gate voltage when the sample is magnetized in the opposite direction and all electrodes are grounded. Similarly, there is no significant change in the static flux signal.

These data indicate that in our experiments, the magnetization of $MnBi_2Te_4$ does not change with variations in the back gate voltage or the spatial distribution of the sample current.

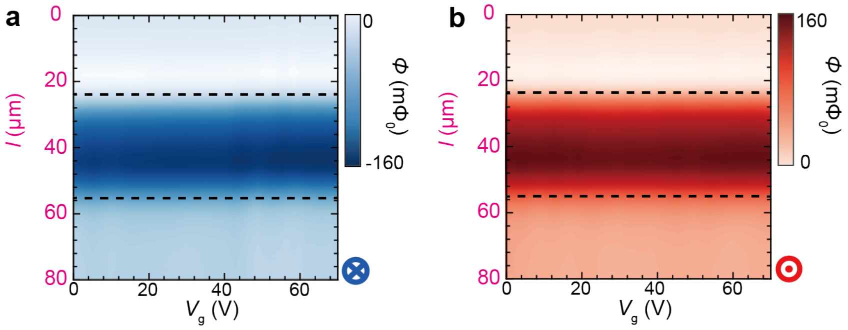

FIG. S17 Gate voltage evolution of static magnetization of device#1. **a**, Gate voltage dependence of the static flux line-cut of device#1 along the magenta dashed arrow in Figure 3a with an AC 500 nA + DC 1 μA current passing through the device. the device is magnetized at -9 T in **a**. **b**, Gate voltage dependence of the static flux line-cut of device#1 along the magenta dashed arrow in Figure 3a with all device electrode grounded and a modulation voltage applied to the back gate electrode as introduced in Figure S18. The device is magnetized at +9 T in **b**. The dashed black lines in **a** and **b** indicate the upper and lower edge of the 7-SL $MnBi_2Te_4$ flake in device#1.

S16: Elimination of electric coupling induced artifacts

The electric coupling between the scanning SQUID and a back gate-tuned magnetic sample can lead to a gate-voltage dependent artifact when imaging the magnetic response to an applied current (dΦ/dI) or voltage (dΦ/dV), as reported by Spanton, et al [23]. The electric coupling artifact in dΦ/dV and dΦ/dI images would cloud the intrinsic chiral edge current feature in a ferromagnetic sample. Hence, here we conduct a careful examination of the artifact induced by the electric coupling.

During the scanning process, the SQUID's pick-up coil is brought very close to the sample ($1\mu m$ above the sample in our case), and the pick-up coil and its shielding are grounded during normal operation of the SQUID. Thus, a charge on the sample will exert a Coulomb force on a grounded metallic SQUID. A back gate voltage can tune the charge accumulated on the sample, and an AC current or voltage applied to the sample modulate the charge at the applied current /voltage frequency. If the SQUID chip is mounted to an easy to deformation base (on a copper cantilever as shown in ref. 19), the Coulomb force will lead to a deflection of the SQUID at the frequency of the current passing through the sample. For a ferromagnetic sample, this electric coupling artifact will produce CEC like current flux feature at the sample edge and domain wall boundary inside the sample.

From the above introduction, we can understand that the appearance of artifacts caused by electric coupling requires three prerequisites: 1. The sample is between the gate electrode and the SQUID, i.e., the back gate is used to tune the sample's Fermi surface. 2. The SQUID is mounted on a deformable substrate. 3. The sample exhibits ferromagnetic properties. In our experiment, we meet the first and third prerequisites among the three mentioned conditions, but not the second one. We have mounted the SQUID onto the cantilever of a quartz tuning fork (TF), and significant changes in the amplitude and phase of the quartz tuning fork occur when the SQUID makes contact with the sample, serving as height feedback [24]. Compared to copper cantilever, quartz tuning fork is less prone to deformation, so it should be less affected by the capacitive coupling between the charge on sample and the SQUID than systems using copper cantilever capacitive bridges.

Magnetic response of back gate voltage modulation

In order to quantitatively analyze the extent to which our current flux signals are affected by electric coupling, we grounded all electrodes of the Device#1 and applied an AC modulation voltage to the back gate (amplitude 0.25 V, frequency 155.55 Hz), as illustrated in Figure S18a. Concurrently, we measured the magnetic response Φ_{V} and the tuning fork amplitude A_{V} at the modulation frequency, as all sample electrodes were grounded, Φ_{V} could directly capture the magnetic response possibly induced by electric coupling without being affected by current flux signals generated by electric currents. A_{V}, on the other hand, directly reflects the magnitude of the Coulomb force of charges on the sample acting on the SQUID. Figures S18b and c show the gate voltage evolution of the magnetic response Φ_V and tuning fork amplitude A_V, respectively. It can be observed that throughout the entire range of gate voltage DC offset, both Φ_V and A_V exhibit signals at the noise level, without any characteristic signals resembling chiral edge current (CEC). This indicates that in our measurements, artifacts induced by electric coupling have no significant impact on our current flux signals. We also performed Φ_V imaging of the entire sample area at back gate voltage DC offsets (V_g = 40 V / 50 V / 60 V, respectively, and observed no noticeable magnetic response induced by electric coupling when the sample Fermi level is in the valence band (V_g = 40 V, Figure S18d), bandgap (V_g = 50 V, Figure S18e), or conduction band (V_g = 60 V, Figure S18f). Based on the above analysis, we conclude that the deformation caused by the Coulomb force of electric coupling on the Quartz tuning fork at low temperatures is too small, resulting in very minor artifact signals induced by electric coupling in our current flux images, which do not affect our results regarding chiral edge current.

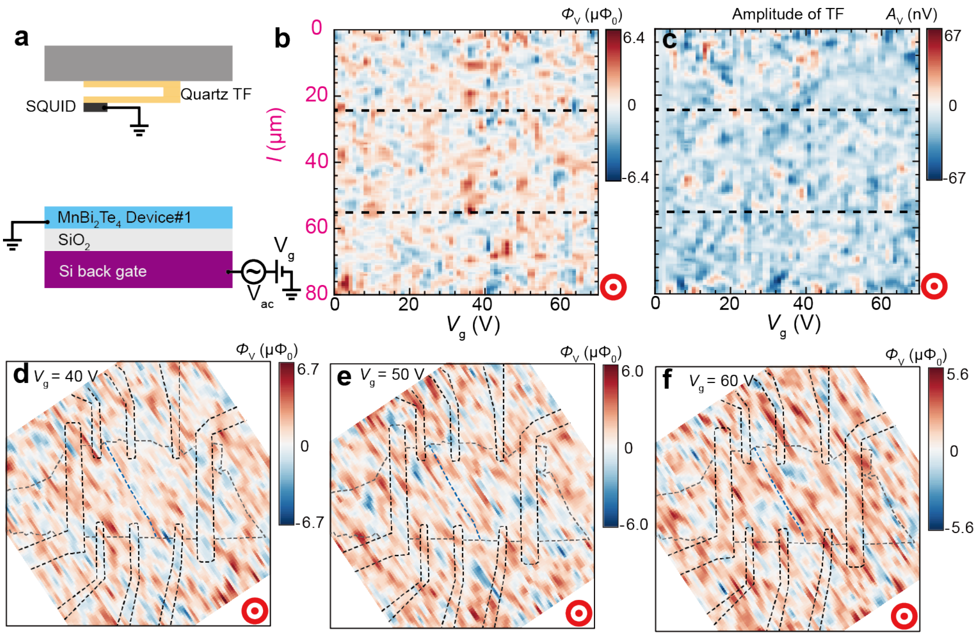

FIG. S18 Exclusion of electric coupling induced artifacts. **a**, Schematic of the measurement. **b** and **c**, Gate voltage evolution of the magnetic response Φ_V and amplitude of the TF A_V at the gate modulation frequency read out by the lock-in amplifier, respectively. A_V can quantitatively reflect the electric force exerted on the TF induced by the electric coupling between the FM sample and SQUID. The black dashed lines indicate the two edges of the 7-SL device#1 along the magenta dashed arrow in Fig. 3a. **d** to **f**, Φ_V images of the entire sample region at V_g = 40 V in **d**, V_g = 50 V in **e** and V_g = 60 V in **f**, respectively.

Frequency dependence of the chiral edge current

The "chiral edge current" artifact induced by electric coupling varies with the frequency of the current applied to the sample due to the mechanical resonance of the SQUID's cantilever. Figure S19 shows the frequency dependence of the chiral edge current signal for device#3 with an AC 500 nA + DC 1 μA current bias applied to the left electrode A and grounded the right electrode D and reversed bias direction. It can be observed that at low current frequencies such as 155.55 Hz (Figures S19a and i), at this point, the current approximates a direct current passing through the sample, so the impedance in the circuit is primarily resistive. Consequently, the main signal in the current flux is concentrated in the real part, with only a minor signal in the imaginary part. As the frequency of the current increases, the capacitive and inductive components of the circuit's impedance become more significant, causing the signal in the imaginary part of the current flux to increase while the signal in the real part gradually decreases.

In our experiments, we used twisted copper wires at room temperature and twisted superconducting wires at low temperatures to apply current to the sample. Therefore, when the current frequency becomes too high, the impedance increases significantly. For the CEC artifact induced by electric coupling, it will be in phase with the magnetic signal generated by the current when the current frequency is below the mechanical resonance frequency of the electric coupling. However, when the current frequency exceeds the resonance frequency, the electric coupling-induced artifact should be out of phase with the magnetic signal generated by the current. This means that in the current flux image, the edge through which the current flows would shift from the upper edge, as shown in Figure S19a, to the lower edge.

In our experiments, across all applied current frequencies, we do not observe any changes in the edge through which the current flows in the current flux image. This indicates that the electric coupling does not significantly affect the CEC signal in our measurements.

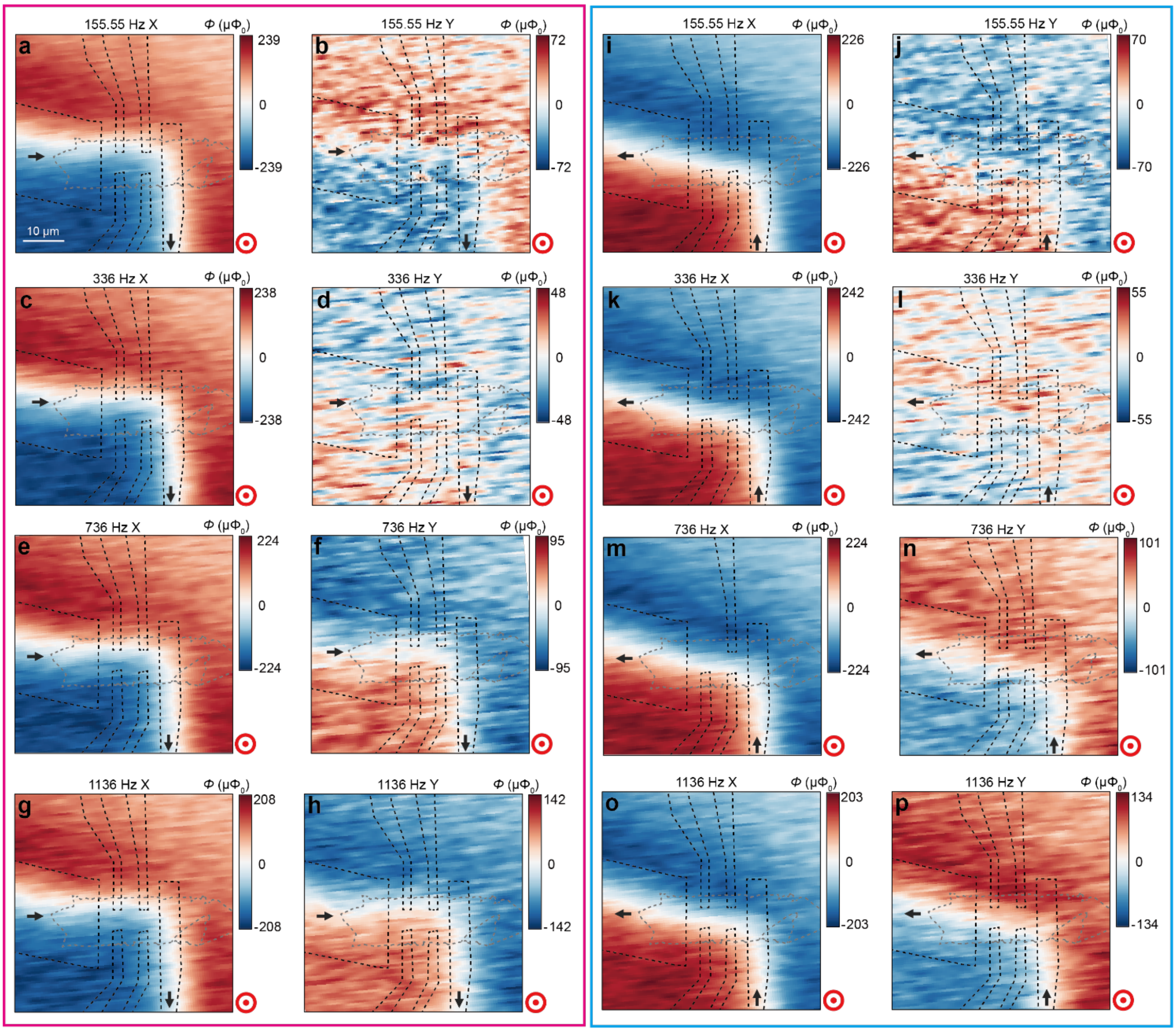

FIG. S19 Frequency dependence of the chiral edge current in device#3. An AC 500 nA + DC 1 μA current bias is applied to the left electrode A and the right electrode D is grounded for panels **a** to **h** in the magenta rectangular, and reversed current direction for panels **i** to **p** in the cyan rectangular. The frequency of the AC current bias is labeled on the top of each figure panel and the back gate voltage $V_g = 5$ V.

Reference

[1] K. C. Nowack et al., *Imaging Currents in HgTe Quantum Wells in the Quantum Spin Hall Regime*, Nat. Mater. **12**, 787 (2013).

[2] A. Y. Meltzer, E. Levin, and E. Zeldov, *Direct Reconstruction of Two-Dimensional Currents in Thin Films from Magnetic-Field Measurements*, (2017).

[3] T. Ando, Y. Matsumoto, and Y. Uemura, *Theory of Hall Effect in a Two-Dimensional Electron System*, J. Phys. Soc. Jpn. **39**, 279 (1975).

[4] K. v. Klitzing, G. Dorda, and M. Pepper, *New Method for High-Accuracy Determination of the Fine-Structure Constant Based on Quantized Hall Resistance*, Phys. Rev. Lett. **45**, 494 (1980).

[5] R. B. Laughlin, *Quantized Hall Conductivity in Two Dimensions*, Phys. Rev. B **23**, 5632 (1981).

[6] X.-L. Qi, T. L. Hughes, and S.-C. Zhang, *Topological Field Theory of Time-Reversal Invariant Insulators*, Phys. Rev. B **78**, 195424 (2008).

[7] B. I. Halperin, *Quantized Hall Conductance, Current-Carrying Edge States, and the Existence of Extended States in a Two-Dimensional Disordered Potential*, Phys. Rev. B **25**, 2185 (1982).

[8] R. Kubo, *A General Expression for the Conductivity Tensor*, Can. J. Phys. **34**, 1274 (1956).

[9] D. J. Thouless, M. Kohmoto, M. P. Nightingale, and M. den Nijs, *Quantized Hall Conductance in a Two-Dimensional Periodic Potential*, Phys. Rev. Lett. **49**, 405 (1982).

[10] D. J. Thouless, *Quantization of Particle Transport*, Phys. Rev. B **27**, 6083 (1983).

[11] Q. Niu, D. J. Thouless, and Y.-S. Wu, *Quantized Hall Conductance as a Topological Invariant*, Phys. Rev. B **31**, 3372 (1985).

[12] Y. Hatsugai, *Chern Number and Edge States in the Integer Quantum Hall Effect*, Phys. Rev. Lett. **71**, 3697 (1993).

[13] M. Büttiker, *Absence of Backscattering in the Quantum Hall Effect in Multiprobe Conductors*, Phys. Rev. B **38**, 9375 (1988).

[14] Y. Imry, *On Macroscopic Quantum Phenomena Associated with the Quantised Hall Effect*, J. Phys. C Solid State Phys. **16**, 3501 (1983).

[15] M. Büttiker, Y. Imry, and R. Landauer, *Josephson Behavior in Small Normal One-Dimensional Rings*, Phys. Lett. A **96**, 365 (1983).

[16] G. M. Ferguson, *Direct Visualization of Electronic Transport in a Quantum Anomalous Hall Insulator*, Nat. Mater. **22**, (2023).

[17] I. T. Rosen, M. P. Andersen, L. K. Rodenbach, L. Tai, P. Zhang, K. L. Wang, M. A. Kastner, and D. Goldhaber-Gordon, *Measured Potential Profile in a Quantum Anomalous Hall System Suggests Bulk-Dominated Current Flow*, Phys. Rev. Lett. **129**, 246602 (2022).

[18] Y. Bai et al., *Quantized Anomalous Hall Resistivity Achieved in Molecular Beam Epitaxy-Grown MnBi2Te4 Thin Films*, Natl. Sci. Rev. nwad189 (2023).

[19] S. Zhang et al., *Experimental Observation of the Gate-Controlled Reversal of the Anomalous Hall Effect in the Intrinsic Magnetic Topological Insulator MnBi $_2$ Te $_4$ Device*, Nano Lett. **20**, 709 (2020).

[20] S. Yang et al., *Odd-Even Layer-Number Effect and Layer-Dependent Magnetic Phase Diagrams in \mathrmMnBi_2\mathrmTe_4*, Phys Rev X **11**, 011003 (2021).

[21] Z. Lian et al., *Antiferromagnetic Quantum Anomalous Hall Effect Modulated by Spin Flips and Flops*, (2024).

[22] S. K. Chong, *Intrinsic Exchange Biased Anomalous Hall Effect in an Uncompensated Antiferromagnet MnBi2Te4*, Nat. Commun. (2024).

[23] E. M. Spanton, A. J. Rosenberg, Y. H. Wang, J. R. Kirtley, F. Katmis, P. Jarillo-Herrero, J. S. Moodera, and K. A. Moler, *Electric Coupling in Scanning SQUID Measurements*, Science **349**, 948 (2015).

[24] Y. P. Pan, J. J. Zhu, Y. Feng, Y. S. Lin, H. B. Wang, X. Y. Liu, H. Jin, Z. Wang, L. Chen, and Y. H. Wang, *Improving Spatial Resolution of Scanning SQUID Microscopy with an On-Chip Design*, Supercond. Sci. Technol. **34**, 115011 (2021).